Kõrgesaar, Mihkel; Romanoff, Jani; Remes, Heikki; Palokangas, Pekka

Experimental and numerical penetration response of laser-welded stiffened panels

Published in:
International Journal of Impact Engineering

DOI:
10.1016/j.ijimpeng.2017.12.014

Published: 01/04/2018

Document Version
Publisher's PDF, also known as Version of record

International Journal of Impact Engineering 114 (2018) 78–92

Contents lists available at ScienceDirect

International Journal of Impact Engineering

journal homepage: www.elsevier.com/locate/ijimpeng

Experimental and numerical penetration response of laser-welded stiffened panels

Mihkel Kõrgesaar[a,*], Jani Romanoff[a], Heikki Remes[a], Pekka Palokangas[b]

[a] Aalto University, School of Engineering, Department of Mechanical Engineering, PO BOX 14300, FI-00076 Aalto, Finland
[b] Alten Finland, Kivikonkierto 18, FI-05460, Hyvinkää, Finland

ARTICLE INFO

Keywords:
Panel indentation
Stiffened panel
Ductile fracture
Tensile testing
Fracture simulations

ABSTRACT

Ductile fracture in large structures is often resolved with non-linear finite element (FE) simulations employing structural shell elements which are larger than localization zone. This makes solution element size dependent and calibration of material parameters complex. Therefore, the paper explores the ability of numerical simulations to capture the penetration resistance of stiffened panels after determining steel material fracture ductility at different stress states. The numerical simulations are compared with experiments performed with rigidly fixed 1.2 m square panels penetrated with half-sphere indenter until fracture took place. Response of the panels was measured in terms of indentation force versus indenter displacement. In parallel, tensile tests were performed with four different flat specimens extracted from the face sheet of panels to characterize the material fracture ductility at different stress states. Panel simulations were performed with two fracture criteria: one calibrated based on the test data from dog-bone specimen and other calibrated based on the data from all tensile tests. To evaluate the fracture criteria in terms of their capacity to handle mesh size variations, mesh size was varied from fine to coarse. Results suggest that fracture criterion calibrated based on the range of stress states can handle mesh size variations more effectively as displacement to fracture showed considerably weaker mesh size dependence.

1. Introduction

1.1. Background

Growing awareness of environmental risks related to storage and transportation of chemicals and fossil fuels provides strong incentive to develop impact and collision resistance structures. Thin-walled structures such as ships transporting hazardous substances are especially vulnerable to puncture due to the collision and grounding that constitute as the most frequent accident type [1]. Resulting chemical or oil spill poses a devastating effect on the marine ecosystem [2], but also involves high acute costs through clean-up operations especially in remote and sensitive areas [3] in addition to indirect effect to economic activities in the region [4].

While the pre-emptive risk management approaches and analyzes are the most effective means to combat the occurrence of these accidents [5–7], the performance of the ship structure during the accident determines the degree of seriousness and consequence. Therefore, understanding the whole damage process under localized loads and ability to simulate fracture in large thin-walled structures is a crucial step from mere assessment of structural failure, towards structures where material fracture is carefully engineered to occur in a desired, well controlled manner. Moreover, this understanding lends itself for successful holistic safety assessment procedure including post-accidental flooding simulation where size of the opening plays an important role [8,9].

Therefore, penetration resistance of stiffened steel plates has been extensively studied experimentally and numerically. Recent review by Calle and Alves [10] covering numerical material fracture modelling approaches in ship crash analysis highlights the high computational cost of the analysis and consequent restriction to large structural shell elements. While computationally efficient, the size of the large structural shell elements imposes restrictions on how the fracture initiation and propagation can be modelled in large structures [11]. When shell elements are used together with element erosion technique to represent fracture, the main challenge is to select the appropriate numerical fracture strain as it depends on the element size and stress state. For instance, benchmark analysis by Storheim et al. [12] where simulations and experiments of three different stiffened shell structures were compared showed that fracture criteria are in general not sufficiently accurate with respect to the stress-state and mesh dependence.

* Corresponding author.
E-mail address: mihkel.korgesaar@aalto.fi (M. Kõrgesaar).

https://doi.org/10.1016/j.ijimpeng.2017.12.014
Received 17 July 2017; Received in revised form 7 November 2017; Accepted 14 December 2017
Available online 15 December 2017

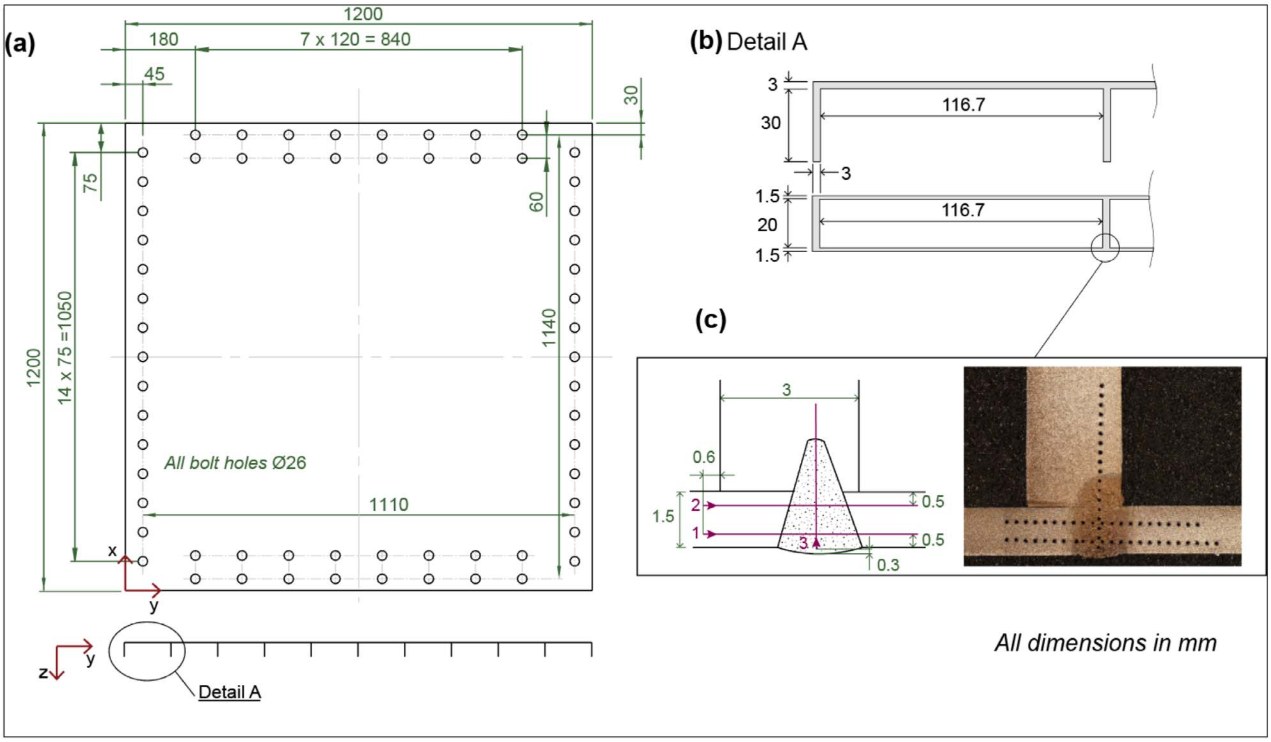

Fig. 1. (a) Geometry and dimensions of stiffened panel. (b) Cross-section of the stiffened panel and similar sandwich panel. (c) Detailed view of laser stake weld showing the three hardness measurement locations.

One factor that contributes to the large scatter in results is the lack of experimental data where both, material and structural behaviour, are readily available. Clearly, the full-scale ship collision and grounding experiments are invaluable in providing the insight to the whole collision process [13,14], but the high cost and difficulty of separating internal and external mechanics makes detailed damage and deformation mode assessment unreliable. Instead, structural tests with scaled structures are preferred where penetration resistance of structures is assessed in controlled laboratory environment, e.g. see the review by Calle and Alves [10] and more recent experimental-numerical investigations by Morin et al. [15] and Gruben et al. [16]. Although these tests map the most important failure modes observed in full-scale experiments, including the fracture under different stress states, accompanying tensile tests were performed only under uniaxial tension. Thereby, fracture strain used in simulations ignored the effect of stress state [17,18] or stress state effect was calibrated only based on uniaxial tensile test, e.g. [19,20]. Moreover, fracture strain sensitivity to element size (mesh size dependence) is also established based on the single stress state, although it is well established that mesh size dependence relates to the amount of strain localization prior to fracture and thus, depends on the stress state. Consequently, in these attempts to resolve fracture strain scaling based on a single stress state lead to inconsistent results with respect to discretization. While calibration based on single test is efficient and attractive especially in design practice, the objective of this work is to show the enhanced consistency, and thus reliability, of the FE solution when fracture strain and its element size sensitivity is calibrated based on different tensile tests.

Therefore, we experimentally determined the penetration resistance of laser welded stiffened steel panels deformed quasi-statically with rigid indenter and performed tensile tests that cover range of stress states. Stiffened panels are common structural elements in ship and offshore structures. Tensile tests were repeated at least twice to check the validity of the experimental set-up, and thus confirm the repeatability of the tests. Data acquisition in panel experiments comprised indentation force and displacement of the indenter. Although material ductility in heat affected zone can considerably change compared with base material, the present investigation is limited to fracture in base plate.

1.2. Limitations

The main motivation for the paper is to test the fidelity of existing FE simulation approaches for bridging the fracture ductility information from small coupon scale tests to large structural components. This relates to the concern for low velocity ship collision impacts. However, the investigation excludes the strain rate effect to the extent where effect can be observed on material behaviour and dynamic effects on the deformation mode. Such a quasi-static analysis method is often used and justified in engineering practice when the principal features of structural response under low velocity impact are well captured by the quasi-static method [21]. In the latter, it is demonstrated in that error of quasi-static analyses in beam impact problem reduces with increasing mass ratio between striking and struck object. Adopting the same principle to a 90-degree ship collision between two similar size ships, might suggest why most of the ship collision analysis neglects the dynamic effects, see e.g. [22]. For all the practical purposes, it is reasonable to approximate the mass of the striking ship much higher, since the mass of the struck ship can be approximated by the mass of the confined region between rigid bulkheads that is damaged during the collision event. Strain rate effects, on the other hand, are excluded because of the lack of robust method which formulates the combined effects of element length, stress triaxiality and strain rate on the ductile fracture strain under the plane stress shell element framework. Furthermore, it is generally agreed that in ship collision analysis inclusion of strain-rate effects is detrimental to simulation accuracy without careful calibration [23], and analysis excluding strain-rate effects are conservative as the estimated indentation into the struck vessel decreases with increasing strain-rate hardening that in turn leads to smaller opening size.

2. Experiments

2.1. Laser welded panel design

Laser welded stiffened (SP) steel panels were manufactured by Koneteknologiakeskus in Turku, Finland from steel sheets produced by SSAB. Geometry and theoretical dimensions of panels are shown in Fig. 1. Stiffener spacing is about 120 mm. Face plates and stiffeners are welded together with laser stake welds. Welding laser was 10 kW IPG fiber laser with Precitec YW52 laser welding optics, where collimation length was 200 mm, focusing length 300 mm and process fiber width 200 microns. Welding power was 3–4 kW and speed 2 m/min speed. Before welding long seams, plates were spot welded together. Laser welding is becoming increasingly popular in shipbuilding industry as it allows low levels of welding distortion at high productivity rates [24]. However, highly localized heat input and cooling rates can lead to strength and toughness mismatch between base and weld material, which can affect the joint ductility especially during large deformations and constrained geometries [25]. Therefore, to examine the joint properties, hardness measurements were performed on stake weld cross-sections cut from the sandwich panels produced along with the stiffened panels reported in this paper, see Fig. 2(b). Although the face plate in sandwich panels was 1.5 mm thick, we presume that results are still applicable for stiffened panels. Hardness profile measured from a sandwich panel laser stake weld is shown in Fig. 2. The hardness of weld metal is twice the one measured in base material. Although according to DNV-GL Guidelines in [26] welds are not exceptionally brittle and their behaviour can therefore be assumed ductile, the ductility of the material in HAZ can considerably differ from the base material as shown in [15,27]. Nevertheless, by presuming that hardness linearly correlates with yield and tensile strength of the steel as shown in [28], fracture initiation was anticipated to take place in the base material that was also confirmed by the experiments. Furthermore, since the exact determination of material properties in HAZ would require additional effort, e.g. [29], it is not attempted herein, and the uncertainty related with welds and their modelling is left out of the scope of present investigation.

2.2. Experimental set-up and program

The quasi-static indentation experiments were conducted at the Strength of Material laboratory in Aalto University. Test set-up used in experiments is shown in Fig. 3. Hydraulic force cylinder with capacity of 1MN was mounted with M24 bolts on the middle of the loading frame. Loading frame was installed on two loading plates on the floor, each having load-carrying capacity of 1MN. Applied indentation force was measured with 1MN force transducer connected to bottom end of the force cylinder. Bulb indenter was mounted on force transducer using adapter in between. Adapter was used to shift indenter closer to the panels because of the limited cylinder stroke. Indenter had a polished surface finish. Indenter could rotate during indentation to protect force sensor from bending moments. Four springs were installed between indenter and force sensor to prevent movement of indenter in unloaded position. These springs were enough to suppress the indenter rotations before fracture initiation and even during early stage of fracture propagation.

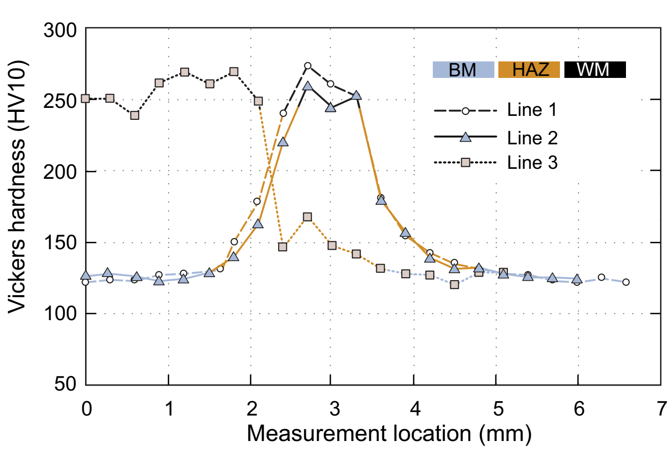

Fig. 2. Hardness profile measured over laser stake weld of sandwich panel. BM refers to base material, HAZ denotes heat affected zone and WM weld material. For definition of lines 1 to 3 see Fig. 1(c). *Y*-axis units HV10 refer to diamond pyramid hardness value under test conditions of 10 kg/mm^2, which can be correlated with yield and tensile strength, see Ref. [28].

Multiple panel experiments motivated a clamping and support design configuration that allowed fast assembly as well as removal of specimens after tests. The assembled configuration is illustrated in Fig. 4(a), where the square panel specimen is fully edge clamped between two picture frame type support plates made from standard structural steel S355. The back-support plate was bolted to an I-beam frame resting on a concrete support base. A 25 mm diameter, 62-hole pattern with internal (female) threads in a back-support plate allowed edge clamping the test panels with top support (clamping) plate. Edge clamping was achieved by 62 M24 bolts (grade 10.9) with external (male) treads without using a traditional nut. A tightening torque of 800Nm was used delivering a total clamping force of ~ 9 MN. Clamping width in all edges was 120 mm resulting in a 960 × 960 mm square centre opening or the exposed area of panels. To avoid collapse of the panels from edges under clamping loads steel inserts were used as supports. Height and width of the inserts was designed to ensure snug fit into the enclosed space. I-beam support frame was built from European wide flange beams (DIN 1025/EN 10034 HE600B) fastened together with grade 8.8 M24 steel bolts using four corner brackets. Additional spacer plates were used between brackets and support frame to adjust the beams into correct positions with respect to each other. FE simulations were performed beforehand to ensure the sufficient stiffness and strength of the frame.

In total 5 tests were performed with stiffened panels, while one panel (SP3) was used for tensile specimen cutting. The full test matrix is shown in Table 1. In the first test (SP1) the indentation location was between 3rd and 4th stiffener (y = 300 mm) from the panel edge. However, in that configuration asymmetric boundary conditions developing during the loading caused excessive indenter rotations due to which we s stopped the test prior to fracture. Therefore, in rest of the tests focus was on the centre indentation and confirming the repeatability of tests. Contact initiation point in tests was verified by pushing the indenter against a piece of Blu–Tack adhesive placed on the panels. Location of the imprint was measured and is reported in Table 1 with respect to the coordinate system in the panel corner (see Fig. 1(a)).

2.3. Measurements

Indenter displacement was measured with HBM WA500 displacement transducer mounted between piston and cylinder. Accuracy of 500 mm sensor was validated with 100 mm sensor (HBM WA100) at small displacements. Vertical deflection of the loading frame was measured with 10 mm HBM WA10 displacement transducer. Movement of force cylinder was displacement controlled during indentation with maximum displacement of 300 mm. To minimize the strain rate effects, indenter velocity was set to 10 mm/min. Penetration was manually stopped in all experiments at the point where indenter started to rotate due to the asymmetric post-failure resistance.

Furthermore, to track the panel deformations during tests two high-speed cameras were installed under the panel, see Fig. 4(b). Cameras used in experiments featured camera body Basler acA2000-340 km and lenses Edmund Optics Techspec #59-870 with 16 mm focal length and #63–243 with 8 mm focal length. Cameras were positioned to capture deformations of the middle of the plate directly under the indenter. The

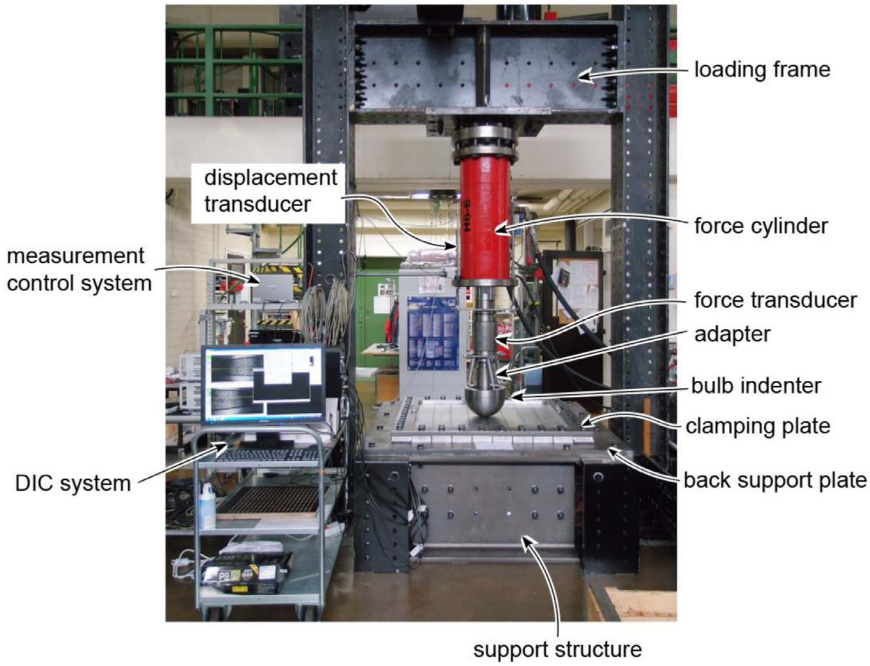

Fig. 3. Overview of the panel test set-up.

16 mm lenses were focused so that the sharpest images were formed on assumed indentation depth determined with preliminary FE simulations. To compensate for inevitable decrease in light due to small aperture and consequent under-exposure, LED lights were assembled inside the support structure. However, first experiments showed that fracture propagated outside of the camera view, thus 8 mm lenses were used instead. Hence, sharp images were obtained throughout the out-of-plane penetration process by maximizing the depth of field with the smallest possible aperture of the lens (f16).

2.4. Tensile tests

Panels are made from standard structural steel S235JR commonly used in shipbuilding. To gain more detailed insight to the material behaviour and characterize its plane stress fracture properties at different stress states a set of tensile tests were performed. While a standard tensile, i.e. dog-bone (DB), specimen shown in Fig. 5(a) is common to characterize material stress-strain behaviour, rest of the specimens were designed to obtain approximately constant stress states throughout the loading history up to the instant of fracture initiation, see [30]. All the specimens were extracted from the face sheets of the panels using band saw machine. The length direction of the specimens corresponds to the direction of stiffeners in panels. The final dimensions were achieved by wire electric discharge machine (EDM).

A central hole (CH) specimen shown in Fig. 5(b) was used to characterize the material ductility under uniaxial tension. Compared with dog-bone specimen (DB) where stress triaxiality ($\eta = \sigma_h/\overline{\sigma}$, mean stress divided by equivalent von Mises stress) shifts from uniaxial tension (1/3) at the point of necking to plane strain tension ($1/\sqrt{3}$) at fracture [31], stress triaxiality in the central hole specimen remains nearly constant as confirmed with the preliminary FE simulations. These simulations also showed that hole dimensions affect the stress triaxiality in the fracture location. The best convergence of triaxiality towards uniaxial tension at the point of fracture was obtained with 4 mm diameter hole following the recommendations of Roth and Mohr [30].

To characterize material at plane strain ($1/\sqrt{3}$), notched tensile (NT) specimen shown in Fig. 5(c) was used. Preliminary FE simulations showed that notch geometry has significant effect on the stress triaxiality at the point of fracture initiation. The final geometry of the notch was obtained by iteratively changing the geometry until the stress triaxiality was close to plane strain tension throughout the loading history.

Shear (S) specimen design shown in Fig. 5(d) was motivated by Roth and Mohr [30] and Till and Hackl [32]. Roth and Mohr [30] showed that resulting fracture strain in the specimen is sensitive to the geometry of the shear gauge section as well as the material properties. Therefore, we used the geometry from [30] optimized for DP590 steel as a "seed". However, the preliminary simulations with this seed geometry led to the neck development outside of the desired gauge section – in the central region of the specimen between the edge cutouts. By increasing the distance x_c from 3.18 mm (seed geometry) to 4.38 mm as shown in Fig. 5(d) we could prevent the neck development outside of the gauge.

Quasi-static tensile tests were performed at room temperature with 3 mm thick specimens using a 100 kN MTS servo-hydraulic universal testing machine with an MTS Teststar Controller for displacement control. Specimen thickness was measured in two locations along the gauge, and the average value is given in Table 2. The cross-head velocity of the actuator ranged from 0.2 mm/min to 2 mm/min, depending on the specimen, see Table 2. During testing, the force (using load cell) and displacement (MTS) were recorded. Additionally, displacement fields on one side of the specimen surface were measured with a high-resolution (2 Mpxl) digital camera Lavision Imager Pro X 2 M equipped with 105 mm Nikon lens at a frequency of 2 Hz. The images were post-processed using a LAVISION digital image correlation (DIC) software to acquire local strain data. The system was set up so that force signal from MTS is included in the DIC measurement data, which enabled correlating the force and displacements signals later in the analysis. DIC measurements require speckle pattern on the measured surface to identify individual points and track their movements. Two alternative approaches were used to create the speckle pattern on the specimen surfaces. First, for easier control of the pattern resolution and thus, adjustment for different field of views, the pattern was printed on a flexible tattoo paper (www.craftycomputerpaper.co.uk) and glued on the specimens' surfaces. Despite its flexibility, later analysis of DIC camera images and displacement fields showed that paper started to peel off and fail before steel material rupture. Therefore, as an alternative speckle generation approach laser printer powder was introduced on the specimen surfaces using a fine steel net (mesh density

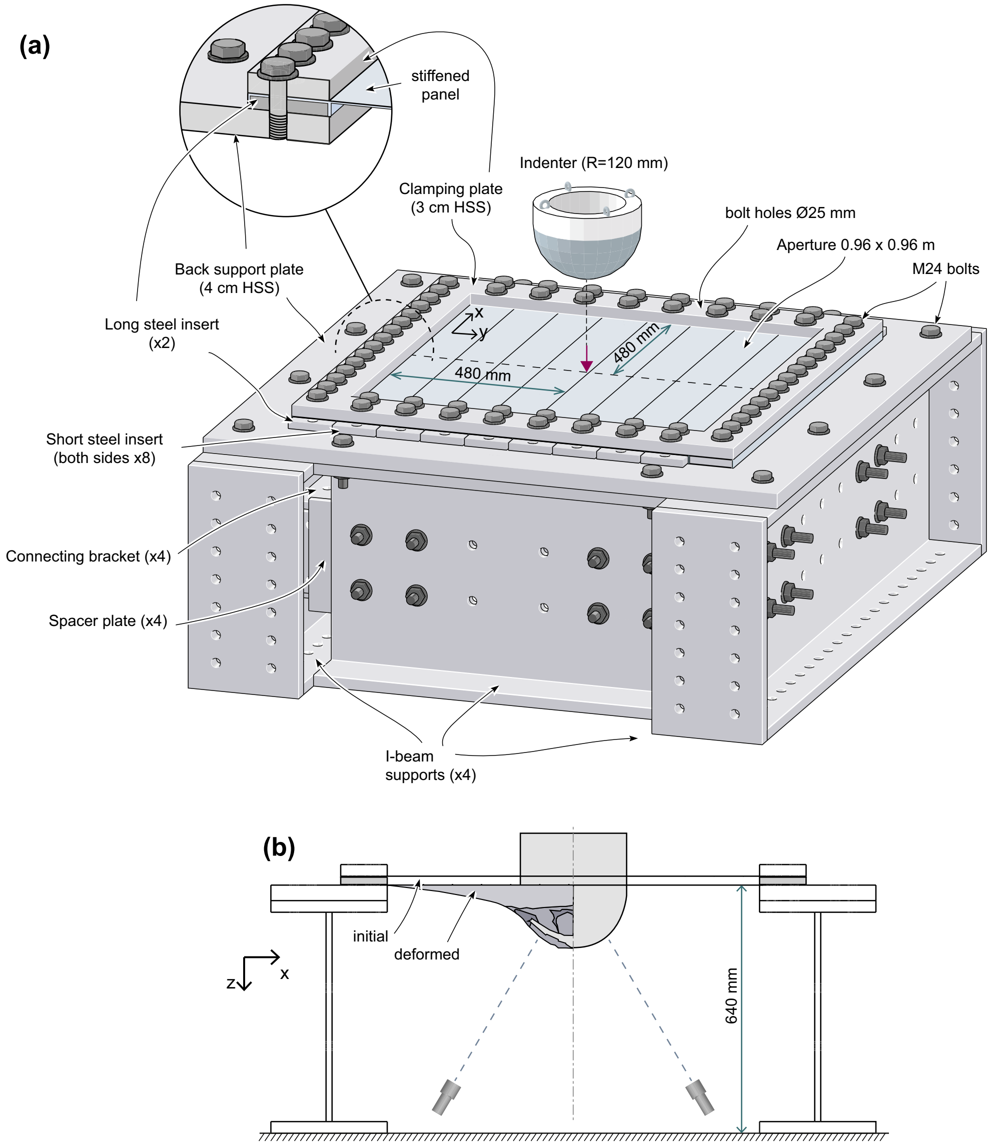

Fig. 4. (a) Stiffened panel fixed to the clamping structure. (b) Side view of the camera positioning (in case of 8 mm lenses).

Table 1
Test matrix.

Specimen ID	Offset from panel corner	
	x (mm)	*y* (mm)
SP1	618	300
SP2	603	595
SP4	598	593
SP5	597	592
SP6	597	593

of 0.125 mm), which was permanently embedded on the surface upon heating the specimens in the furnace ~30 min under 150°. Drawback of this method is that there is limited control over the quality of the pattern, which sometimes included larger inclusions with multiple speckles overlapping, or conversely, whitespaces, where speckle density was scarce. Moreover, analysis of camera images showed that this approach was also unreliable at large strains as speckles came loose from the specimen surface. An example of this is presented in Fig. 6 (a) and (b) where one relatively large speckle jumps from one position to another in consecutive frames. The final frame of the fractured specimen in Fig. 6(c) shows that the pattern has been completely lost.

2.5. Experimental results

2.5.1. Tensile tests

Force-displacement (F-δ) curves of the tensile tests corresponding to each specimen (servo-hydraulic test machine) are shown in Fig. 7. Additionally, for dog-bone (DB) and notched tension (NT) specimens F-δ curves are determined with DIC analyses corresponding to specific virtual gauge length shown on the figure. DIC analyses of central-hole (CH) and shear (S) specimens were unsuccessful for reasons discussed in the previous section and thus, are not shown. In general, specimens display good repeatability with respect to force-elongation and displacement to fracture. The response shows a yield plateau clearly observable from DB specimen response. In CH specimens, this yield plateau leads to a distinctive peak-slump feature at the initial stage of deformation. For each specimen, a selected camera image identified with marker ① in a F-δ curve is shown overlaid with finite element simulation results and/or contours from DIC analyses. In CH specimens, fracture initiation is preceded by the width reduction (diffuse necking) on both sides of the hole. Fracture initiated from the hole boundary where cross-section was the smallest and gradually propagated, as indicated also by the slope of the F-δ curves in the final stage, outside towards specimen edges. The camera image was selected based on the load drop at displacement ①, which was considered a good indicator for

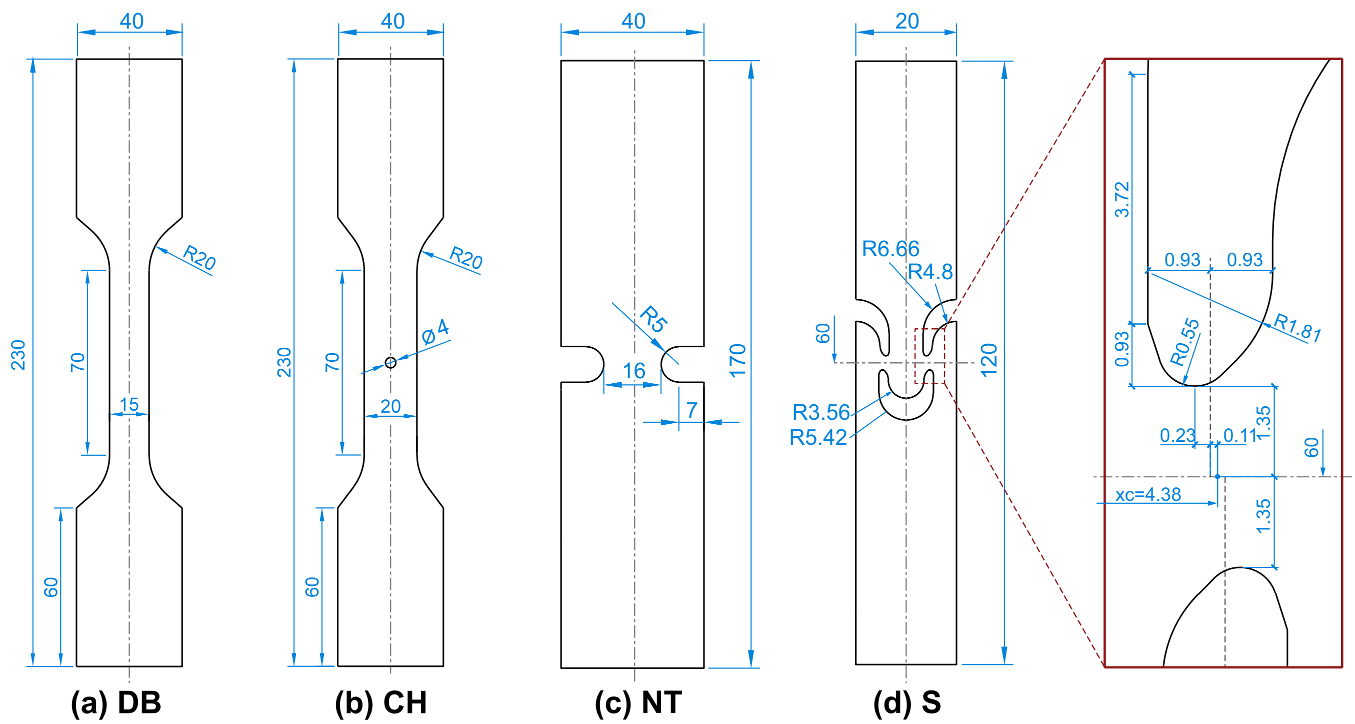

Fig. 5. Specimens used in the study to characterize the material behaviour under different stress states. (a) Standard tensile or dog-bone specimen (DB), (b) central-hole (CH), (c) notched tensile (NT), and (d) shear (S) specimen.

fracture initiation. The corresponding step in simulation was selected based on the perfect agreement between deformed shapes of tested and simulated geometries in Fig. 7(a). At the succeeding FE step this agreement was considerably worse. The displacement difference at point ① between simulation and experiment can be explained by the differences observed in elastic loading stage. In NT specimens, the localized neck development was clearly observable from video analysis as the bright grey band extending across the width, see Fig. 7(b). The chosen image describes the situation few steps before fracture was detected on surface. The corresponding FE image at displacement ① was chosen again based on the geometry agreement between test and FE image. The reference length of strain calculations is different between FE simulation and DIC analysis that explains the discrepancy in logarithmic strain in Fig. 7(b). We did not attempt to resolve this and relied on comparison between MTS and simulation results in determining the fracture strain. In dog-bone (DB) specimen, the selected camera image at ① was the last frame before DIC analysis became unreliable – the loss of data is already seen on the DIC contour image in Fig. 7(c). Since the fracture on surface was detected later as indicated in the F-δ curve, the selected fracture point in simulation does not correspond with the point ①. Instead, the fracture in simulations was assumed to occur at the last simulation step. In shear (S) specimen, the point ① is selected based on the final converged solution of the FE simulation to enable the comparison of deformed configurations. As a general observation applicable to all tests, it should be noted that it is difficult to determine the exact point of initiation and thus, fracture displacements determined in a way described have some error associated with them, e.g. see the discussion in [33]. Nevertheless, the error analysis was deemed unnecessary for the current application where the final objective is to capture the response in large panels.

2.5.2. *Stiffened panels*

Measured force-displacement (F-δ) relations in Fig. 8 indicate to excellent test repeatability as curves practically overlap. Precipitous drop in load suggests that panel response before fracture initiation is dominated by the membrane stretching. Fracture initiation occurs approximately at 180 mm indenter displacement and load of 550 kN at which point panel loses about 60% of its resistance. The second test (SP2) was only partly successful, presumably because of the improper assembly of the support structure. Consequently, force signal exhibits a jump at the indenter displacement of about 55 mm, but final fracture displacement is still very similar to other measurements. After subsequent re-assembly of the set-up this problem was resolved.

Damaged panels are shown in Fig. 9. Despite of the very similar load

Table 2
Test matrix for tensile specimens.

Specimen id.	Thickness [mm]	Width gauge [mm]	DIC pattern	Loading speed [mm/min]	Step [pixel]	Resolution [mm/pixel]	Subset size [pixels]
DB-1-3	2.98	15.08	Print	2	5	0.072	39
DB-2-3	2.99	15.04	Spray	2	5	0.072	39
CH-1-3	3.01	20.05	Spray	1	5	0.014	39
CH-2-3	3.00	20.02	Spray	1	5	0.014	39
CH-3-3	2.99	20.01	Spray	1	5	0.014	39
NT-1-3	3.00	–	Print	0.2	5	0.015	39
NT-2-3	3.00	–	Print	0.2	5	0.015	39
NT-3-3	3.00	–	Spray	0.2	5	0.015	39
S1-3	3.01	–	Spray	0.2	5	0.014	29
S3-3	3.01	–	Spray	0.2	5	0.014	29

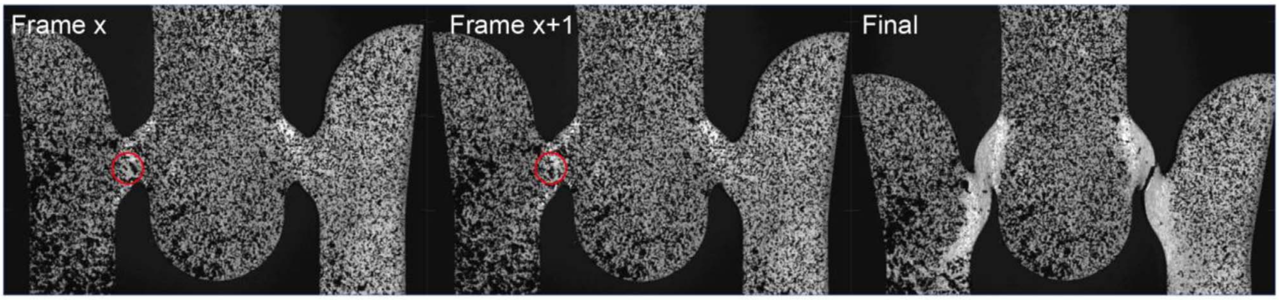

Fig. 6. Image frames captured during S3-1 experiment illustrating the issues with speckle pattern created using laser printer powder. First two images are from consecutive frames and highlight the sudden movement of one, relatively large speckle from one position to another. Last frame shows how pattern has been completely lost after final fracture.

and displacement response, neck development and consequently the final fracture path varied between tests. The final crack path is similar for SP4 and SP6, although in SP4 panel fracture initiated in two locations. First crack initiated in the plate field between two stiffeners and propagated longitudinally. Upon further loading it was accompanied by the second independent crack that extended transversally across the stiffener as shown in Fig. 9(a). Initially this second crack remained in the plate field, but eventually stiffener was fractured as well. In contrast to SP4 and SP6, fracture in SP5 panel initiated on the opposite side of the stiffener where initial contact between indenter and plate occurred, see Fig. 9(b). The point of initiation was also closer to the middle stiffener compared with other panels. Thereon, crack underwent almost straight propagation along stiffener direction without any branching. The contrasting response in crack path of the SP5 panel is rationalized as follows. In SP5 panels the pattern that was intended for DIC measurements was, unintentionally, glued on the top side (contact side) of the panel in two rectangular patches. The employed adhesive considerably increased the friction between plate and indenter and thus, it is reasonable to presume that this is responsible for the different fracture path. Similar contrasting effect of friction on fracture path is often observed in punch experiments with and without lubricants.

Fig. 10 shows the damaged section of the SP4 panel that was cut out. The high stiffness of the laser weld is obvious as weld has remained intact. Stiffener has necked considerably before fracture as demonstrated by the severe thinning, which based on the comparison with intact tensile specimen could be in the range of 50%.

3. Numerical simulations

3.1. Material model

Equivalent stress - equivalent plastic strain curve ($\bar{\sigma} - \bar{\varepsilon}$) up to large strains is necessary input for numerical simulations of panel experiments. The $\bar{\sigma} - \bar{\varepsilon}$ curve was determined based on the combined numerical-experimental inverse approach, e.g. [33]. The elastic properties of the materials were described by a Young's modulus of $E = 200$ GPa, Poisson ratio of $\nu = 0.3$, and density of $7850\,\mathrm{kg/m^3}$. von Mises yield criterion was used in the simulations assuming associated plastic flow and isotropic hardening. Strain hardening was described by a Swift model extended by the Cowper–Symonds viscoplastic strengthening factor:

$$\bar{\sigma} = \begin{cases} \sigma_0\left[1 + \left(\frac{\dot{\varepsilon}}{C}\right)^{1/p}\right] \bar{\varepsilon} \le \varepsilon_L \\ K\,(\bar{\varepsilon} + \varepsilon_0)^n\left[1 + \left(\frac{\dot{\varepsilon}}{C}\right)^{1/p}\right] \bar{\varepsilon} > \varepsilon_L \end{cases} \tag{1}$$

where $\dot{\varepsilon}$ is the equivalent plastic strain-rate, $\bar{\varepsilon} = \int \dot{\varepsilon} dt$ is the equivalent plastic strain, σ_0 is the yield stress, and K and n are the parameters governing the work hardening. To account for the existence of the Lüders plateau, the hardening is delayed until the plastic strain reaches the plateau strain ε_L, while the parameter $\varepsilon_0 = (\sigma_0/K)^{1/n} - \varepsilon_L$ enforces continuity of the stress strain curve at $\bar{\varepsilon} = \varepsilon_L$. The parameters C and p define the strain-rate sensitivity of the material. The initial estimate for the hardening curve up to diffuse necking was obtained from the true stress-plastic strain ($\sigma - \varepsilon_p$) curve calculated based on the dog-bone (DB) test response. Engineering stress and strain was calculated as $s = F/A_0$, where F is the measured force and A_0 is the initial cross-sectional area in the gauge section. Engineering strain was calculated as $e = (l\text{-}l_0)/l_0$, where l and l_0 are the current and initial gauge length, respectively. Corresponding true stress and strain are thus obtained as $\sigma = \mathrm{s}(1 + e)$ and $\varepsilon = \ln(1 + e)$, respectively. The logarithmic plastic strain was calculated from $\varepsilon_p = \varepsilon - \sigma/E$. Material flow curve beyond diffuse necking strain was obtained with the aid of numerical simulations of central-hole (CH) specimen because the specimen exhibited largest strains prior to fracture initiation.

Numerical finite element simulations of the CH tests were performed with FE software Abaqus 6.13-3/Standard (implicit solver) using reduced integration solid elements (C3D8R). In developing the FE model, symmetry of the specimen geometry and loading was exploited – 1/8 symmetry (mid-width, -span, and -thickness). In-plane element size in the gauge region at the expected fracture location was 0.1×0.1 as shown in Fig. 12(a) with 10 elements through half-thickness. A prescribed velocity was applied on the edge of the model. The velocity was ramped up from 0 to 0.5 mm/min over the first 20 s of the simulation using a smooth amplitude function. Thereby, the symmetric gauge region experienced the pre-necking strain rate of $3.33{\cdot}10^{-3}\ \mathrm{s}^{-1}$ as in experiment (gauge length where deformations localize is assumed to be here 5 mm). Initial simulations were performed with the flow curve without viscoplastic strengthening. This led to earlier softening compared with test as shown in Fig. 7(a) and motivated the extension of the material relation with strain-rate dependent term. The parameters defining strain-rate sensitivity were iteratively changed from their initial values of $C = 40\ \mathrm{s}^{-1}$ and $p = 5$ characteristic to structural steels [34] while comparing response of CH simulations to measurements. Final chosen parameters are $C = 25\ \mathrm{s}^{-1}$ and $p = 2.5$. The parameters K and n governing the work hardening in Eq. (1) were determined by coupling the Abaqus solver with the optimization toolbox of Matlab (see also [35]), wherein Neldear–Mead algorithm (function fminsearch) was used to minimize the sum of squared difference between the simulated and measured force-displacement curves. Because of the mismatch between elastic stiffness only plastic portion of the curves were compared during optimization. The final parameters are shown in Table 3 below and the corresponding stress-strain curve is shown in Fig. 11.

The flow curve was validated by performing simulations with three other tested specimens. The modelling principles involving discretization, boundary conditions, and loading scheme whereby pre-necking strain-rates are approximately equal to the test conditions were kept the same. Only exception is shear specimen, which was modelled using 1/4 symmetry instead of 1/8 symmetry. All FE models are shown in Fig. 12. The corresponding F-δ curves are compared with measurements in Fig. 7. The best accuracy is exhibited by the CH and DB specimens. In case of NT and S specimen, the peak force is slightly overestimated, but

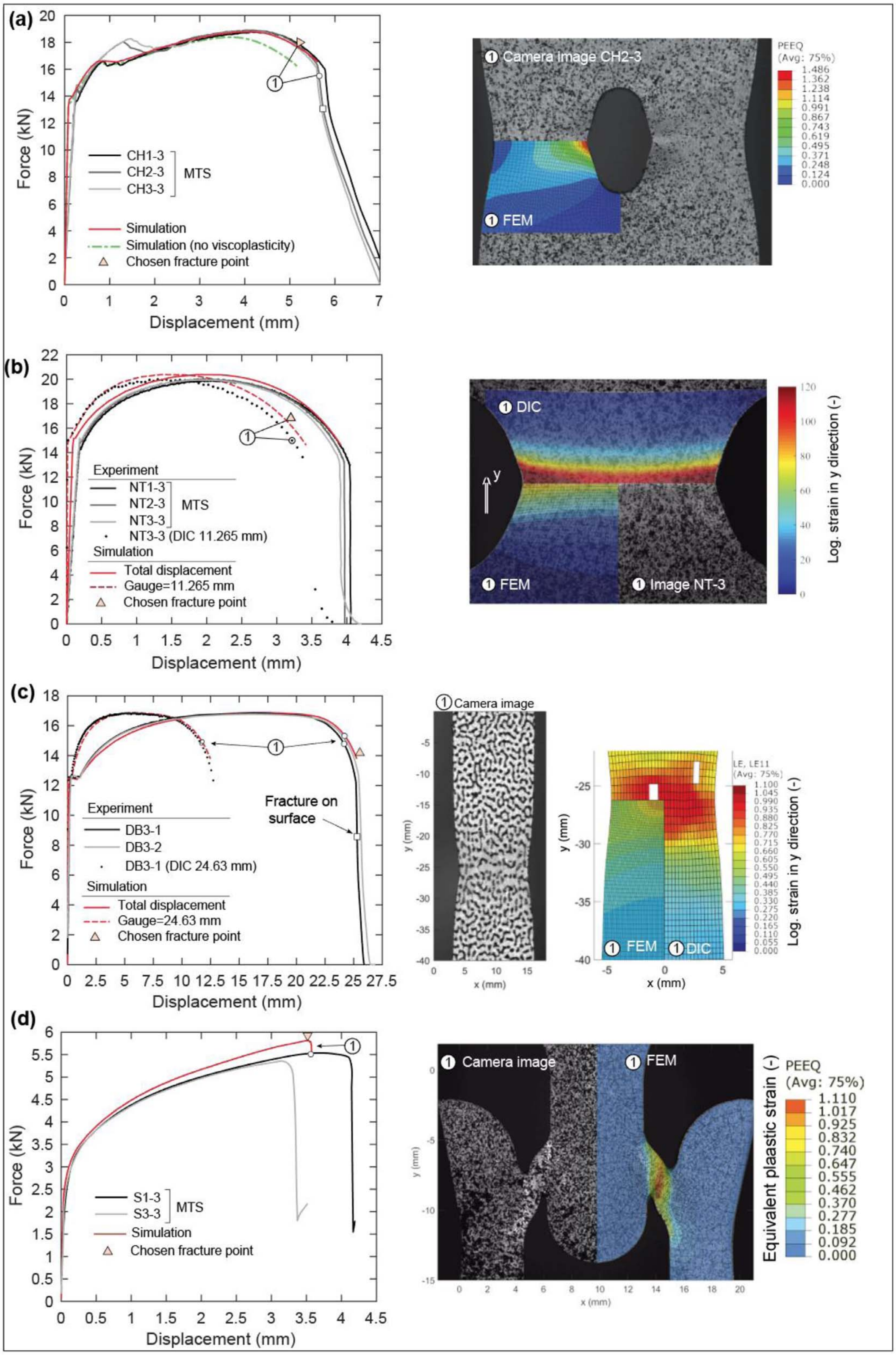

Fig. 7. Force-displacement curves from the (a) central-hole CH, (b) notched tension NT, (c) dog-bone DB, and (d) shear S tests and corresponding FE simulations. The yellow triangular marker corresponds to simulation step based on which equivalent plastic fracture strain was determined. Notice that in right column pictures of (b) and (c) colour contours correspond to logarithmic strain as opposed to equivalent plastic strain shown in the figures (a) and (d). (For interpretation of the references to colour in this figure legend, the reader is referred to the web version of this article.)

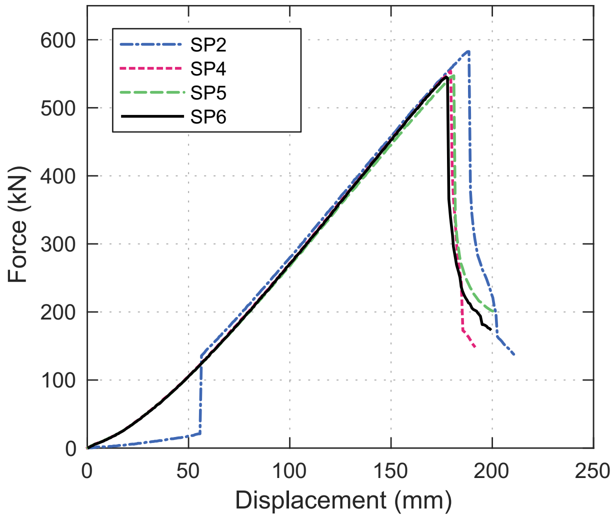

Fig. 8. Measured force-displacement curves of the stiffened panels.

remained within 10% accuracy. This inaccuracy could be potentially reduced by adopting yield criterion that recognises the reduced capacity in plane strain tension [36], but was not attempted here.

3.2. Stress triaxiality dependent fracture strain calibration

To simulate ductile fracture in panels fracture strain dependent on stress triaxiality was calibrated based on the four tensile tests. The equivalent plastic strain at fracture, i.e. fracture strain, was determined based on the F-δ curves shown in Fig. 7 and is marked therein with the triangular marker. Fracture strain in the most critical element in each simulation is plotted as a function of average stress triaxiality ($\bar{\varepsilon}_f - \eta_a$) in Fig. 13 (triangular marker). Average stress triaxiality is calculated with the following integral expression over the load history as it varies throughout the simulation:

$$\eta_a = \frac{1}{\bar{\varepsilon}_f}\int_0^{\bar{\varepsilon}_f} \eta d\bar{\varepsilon} \tag{2}$$

Average stress triaxiality and corresponding fracture strain are gathered in Table 4. Fig. 13 shows that fracture strain is clearly dependent on the specimen type. The notched tension (NT), dog-bone (DB), and shear (S) specimens exhibit almost the same fracture ductility while it is considerably higher in central hole (CH) specimen. Despite the similar average stress triaxiality at failure between DB and CH specimens, the large difference in ductility can be rationalized due to the significantly different loading history experienced by the most critical elements as displayed in Fig. 13. To gauge the sensitivity of the fracture strain due to element size, equivalent plastic strain and stress triaxiality history until fracture are given also for 0.5 mm element length ($\bar{\varepsilon}_{0.5}$, $\eta_{0.5}$). These quantities are obtained by through-thickness averaging of the solid model results over $\sim 0.5 \times 0.5$ mm^2 area:

$$\bar{\varepsilon}_{0.5} = \frac{1}{V}\sum_{i=1}^{n_{el}} \bar{\varepsilon}_i \cdot V_i$$
$$\eta_{0.5} = \frac{1}{V}\sum_{i=1}^{n_{el}} \eta_i \cdot V_i \tag{3}$$

where subscript i is used to distinguish the quantities corresponding to individual elements in models shown in Fig. 12, V denotes volume and n_{el} is the number of elements over which the averaging is performed. The plastic strain history determined this way is also shown in Fig. 13 together with fracture point marked with circular marker. Values are given in Table 4. The chosen volume averaging approach was preferred over shell element simulations as it allowed determining the fracture strain for all cases. When shell element simulations with NT specimens were attempted using 0.5×0.5 mm^2 mesh, a physically unrealistic solution was obtained whereby deformations localized in the single row of elements at the peak load. It is worth mentioning that the volume averaging approach in CH specimen resulted in fracture strain which was the same (difference less than 1%) as obtained with 0.5 mm shell elements.

3.3. Fracture criteria and scaling

One of the motivations of this work is to investigate the accuracy of numerical simulations of large components after material fracture ductility characterization with more than one test. The benefit of multiple tensile tests is insight to stress state dependent material fracture ductility, but how this local material information is bridged to

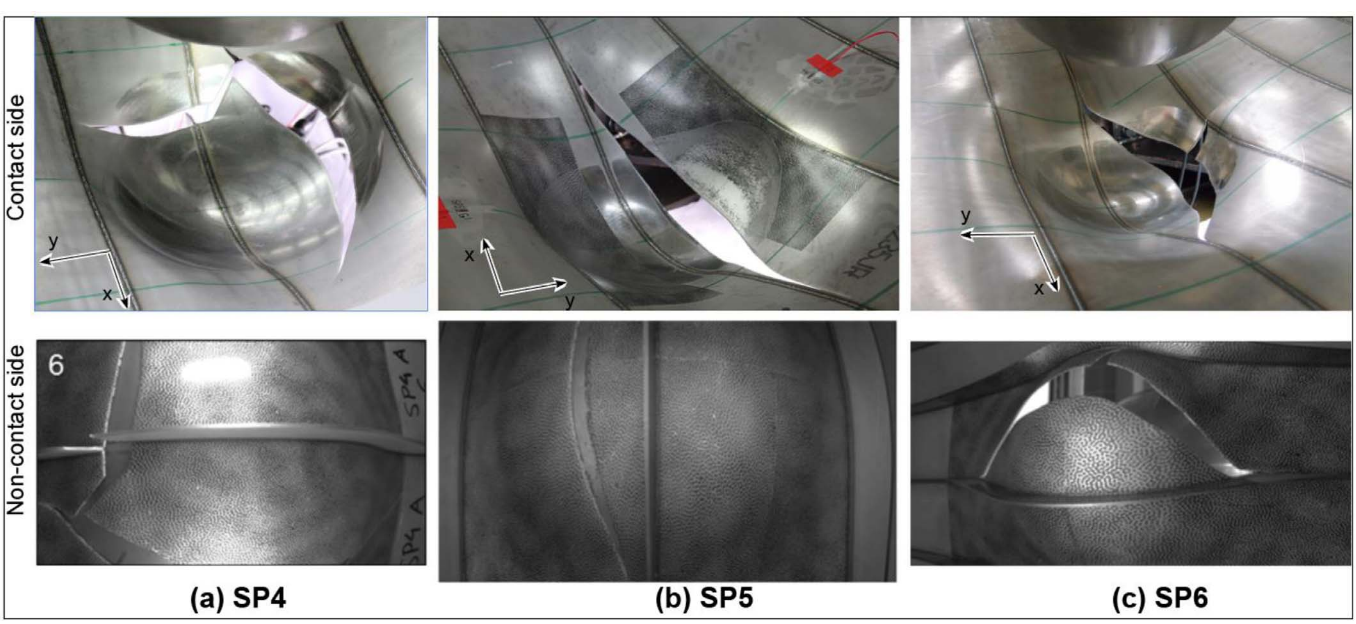

Fig. 9. Fracture has initiated in face plate in all experiments. After initiation, all specimens showed unique crack development. In SP2, crack has grown gradually and broken a stiffener. SP4 fracture has same characteristics but fracture is more circular. Main crack is parallel with the stiffeners whereas second branch goes perpendicularly through a stiffener. SP5 features single smooth crack. Ductile damage mechanism in form of necking can be observed in all specimens.

Fig. 10. Magnification view of the SP4 panel deformed section. (a) Specimen is completely cut into two pieces, but positioned in the photo so that upper part supports on the lower part. (b) Stiffener did not trip and displays a clear neck near the fracture location. (c) 3 mm tensile specimen placed next to the fractured stiffener highlights the significant thickness reduction prior to failure.

Table 3
Material parameters for the hardening model.

σ_0 (MPa)	K (MPa)	n (-)	ε_L(-)	C (s^{-1})	p (-)
275	630	0.21	0.012	25	0.25

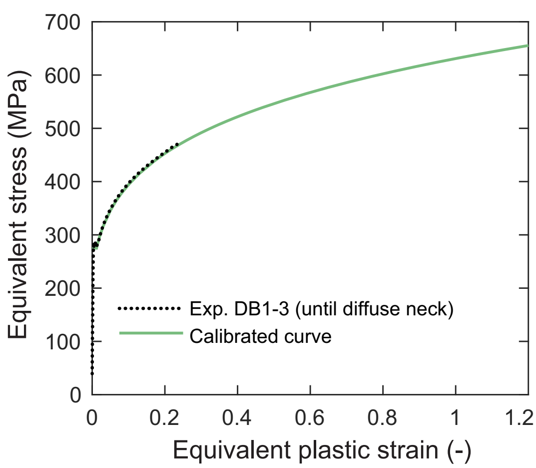

Fig. 11. Equivalent stress-plastic strain curves for standard tensile (dog-bone) samples tested in uniaxial tension to fracture.

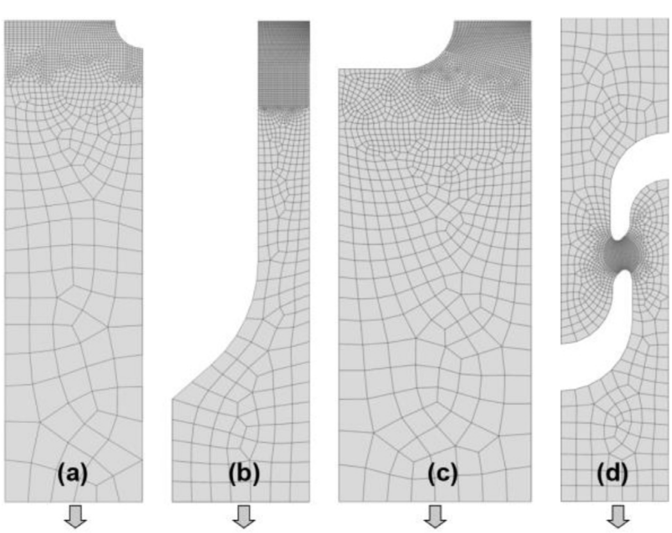

Fig. 12. Symmetric finite element solid models used to validate the hardening curve. (a) Central hole CH, (b) dog-bone DB, (c) notched tension NT, and (d) shear S specimen.

simulations of large structural components is addressed here. In other words, the familiar setting arises where the fracture strain calibrated by tensile tests must be appropriately scaled to consider the mesh dependency of the FE solution. Thereby, accuracy of numerical simulations with large elements depends on the fracture criterion as well as on the fracture strain scaling framework.

3.3.1. Two-factor scaling or 2FS criterion

In this fracture modelling approach fracture strain scaling depends on both the element size (element size take as element length to thickness ratio, L_e/t_e) and stress triaxiality, thus in the following it is denoted as two-factor scaling or 2FS criterion for brevity. We adopt Modified Mohr–Coulomb (MMC) plane stress fracture criterion that is well-established for prediction of fracture in small structural components [37–39]. The criterion is given as in Li et al. [39]:

$$
\begin{aligned}
\bar{\varepsilon}_{MMC} &= \left\{\frac{K}{C_2} f_3 \left[\sqrt{\frac{1+C_1^2}{3}} f_1 + C_1\left(\eta + \frac{f_2}{3}\right)\right]\right\}^{\frac{-1}{n}}\\
f_1 &= \cos\left\{\frac{1}{3}\arcsin\left[\frac{-27}{2}\eta\left(\eta^2 - \frac{1}{3}\right)\right]\right\}\\
f_2 &= \sin\left\{\frac{1}{3}\arcsin\left[\frac{-27}{2}\eta\left(\eta^2 - \frac{1}{3}\right)\right]\right\}\\
f_3 &= C_3 + \frac{\sqrt{3}}{2-\sqrt{3}}(1 - C_3) + (1/f_1 - 1)
\end{aligned}
\tag{4}
$$

where K and n are work hardening parameters given in Table 3 and C_1, C_2, and C_3 are material constants that must be determined to fit the facture loci through fracture data in Fig. 13. These parameters were found by optimization, see Table 5. Optimization was set up so that data points corresponding to DB specimens were neglected to capture the increased fracture ductility exhibited by the CH specimens. Nevertheless, the obtained MMC fracture locus for 0.1 mm length scale still approximates the fracture strain of DB specimens quite well as shown in Fig. 13. For 0.5 mm element length the fitted approximation is less accurate for DB specimen.

The MMC fracture criterion is adjusted for different element lengths according to framework introduced by Walters [40]. The framework considers the fact that mesh size dependence of the fracture strain varies depending on the stress state. In particular, representative volume element simulations in [41] suggested that mesh size dependence under plane strain and equi-biaxial tension are weaker than under uniaxial tension, but more generally, sensitivity of the fracture strain depends on the difference between necking strain and fracture strain. The larger the difference, more sensitive is the FE solution to mesh size. The underlying idea of the framework is to replace the terms in commonly used fracture scaling law for uniaxial tension [42]

$$
\bar{\varepsilon}_f = n + (\bar{\varepsilon}_{UAT} - n)\frac{t_e}{L_e}
\tag{5}
$$

with their stress state dependent counterparts. In Eq. (5) n is the diffuse

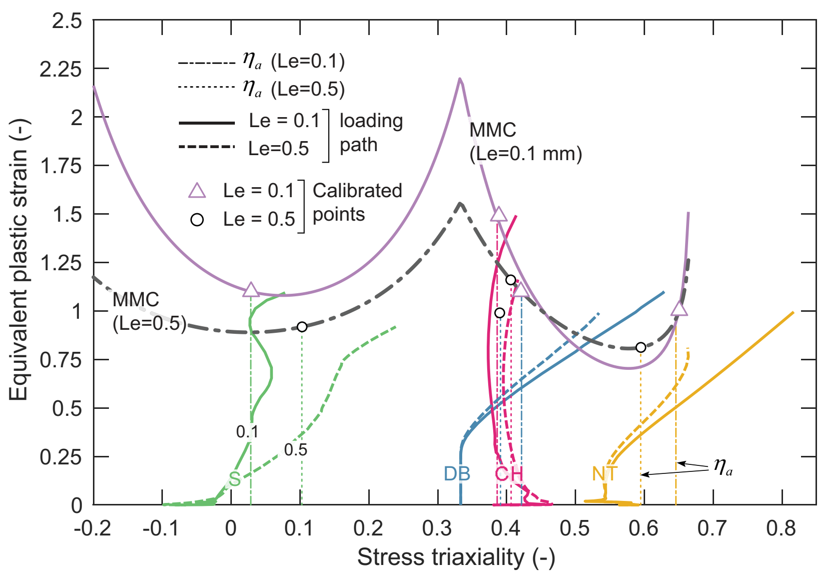

Fig. 13. Fracture strain as a function of stress triaxiality determined using inverse experimental-numerical approach. Figures show also the MMC loci fitted through the data and fracture strain for 0.5 mm elements obtained using volume averaging.

Table 4
Fracture strain and average stress triaxiality determined for two element lengths.

Le (mm)	DB		CH		NT		S	
	η (-)	$\bar{\varepsilon}_f$(-)	η	$\bar{\varepsilon}_f$	η	$\bar{\varepsilon}_f$	η	$\bar{\varepsilon}_f$
0.1	0.422	1.100	0.388	1.486	0.650	0.995	0.029	1.094
0.5[a]	0.390	0.990	0.406	1.160	0.595	0.812	0.103	0.918

[a] Through thickness.

Table 5
Material parameters for MMC fracture loci calibrated based on the fracture strain of CH, NT and S specimens.

L_e (mm)	C_1	C_2	C_3
0.1	0.1059	413.82	1.102
0.5	0.0217	353.49	0.995

necking strain in uniaxial tension (hardening exponent in Table 3) and $\bar{\varepsilon}_{UAT}$ is the fracture strain in uniaxial tension when element length equals plate thickness, i.e., $L_e = t_e$. Walters proposed making Eq. (5) stress triaxiality dependent by replacing the terms as follows:

$$\bar{\varepsilon}_f(\eta, t_e/L_e) = \bar{\varepsilon}_n(\eta) + (\varepsilon^*(\eta) - \bar{\varepsilon}_n(\eta))\frac{t_e}{L_e} \tag{6}$$

where $\bar{\varepsilon}_n(\eta)$ is the diffuse necking strain according to Swift expression and $\varepsilon^*(\eta)$ is the function dependent on the stress triaxiality. This function is expressed from Eq. (6) by

$$\varepsilon^*(\eta) = \bar{\varepsilon}_n(\eta) + (\bar{\varepsilon}_{f,cal}(\eta) - \bar{\varepsilon}_n(\eta))\frac{L_{e,cal}}{t_{e,cal}} \tag{7}$$

where we have replaced $\bar{\varepsilon}_f$ with $\bar{\varepsilon}_{f,cal}(\eta)$ that is the calibrated fracture strain as a function of stress triaxiality, whereas calibration is performed for element length $L_{e,\ cal}$ and thickness $t_{e,\ cal}$. Fracture criterion for plane stress shell elements with length L_e and thickness t_e is thus defined by substitution of this expression into Eq. (6). In place of $\bar{\varepsilon}_{f,cal}(\eta)$ we use the MMC fracture criterion in Eq. (4) fitted to our tensile test data. Since the framework is applicable to shell elements with certain length and thickness, calibration function $\bar{\varepsilon}_{f,cal}(\eta)$ should be associated with the through-thickness fracture strain. Therefore, we adopt the MMC fracture locus corresponding to 0.5 mm elements in Fig. 13, which gives $L_{e,cal} = 0.5$ mm and $t_{e,cal} = 3$ mm.

The triaxiality dependent diffuse necking strain $\bar{\varepsilon}_n(\eta)$ in Eq. (6) represents the lowest fracture strain attainable by the criterion, and thus describes the behaviour of very large elements. The $\bar{\varepsilon}_n(\eta)$ is found from major ε_1 and minor ε_2 principal plastic Swift [43] instability strains assuming a constant stress ratio $\beta = \sigma_2/\sigma_1$

$$\varepsilon_1 = \frac{2(2-\beta)(1-\beta+\beta^2)}{4-3\beta-3\beta^2+4\beta}n$$
$$\varepsilon_2 = \frac{2(2\beta-1)(1-\beta+\beta^2)}{4-3\beta-3\beta^2+4\beta}n \tag{8}$$

Upon assuming plane stress condition and proportional loading, equivalent plastic strain becomes

$$\bar{\varepsilon}_n = \frac{2\varepsilon_1}{\sqrt{3}}\sqrt{1+\alpha+\alpha^2} \tag{9}$$

where $\alpha = \varepsilon_2/\varepsilon_1$ is the strain ratio. In plane stress under the assumption of von Mises flow rule there is one-to-one mapping from stress to strain space that allows relating stress triaxiality to strain ratio

$$\eta = \frac{1}{\sqrt{3}}\frac{1+\alpha}{\sqrt{1+\alpha+\alpha^2}}. \tag{10}$$

However, we found that fracture initiation in very large shells is better approximated when instead of diffuse necking strain n in Eq. (8) (Consider condition, $d\bar{\sigma}/(\bar{\sigma}d\bar{\varepsilon}) = n/\bar{\varepsilon} = 1 \Rightarrow n = \bar{\varepsilon}$), fracture strain is directly calibrated using the existing tensile test data of dog-bone (DB) specimens. Therefore, a single shell element model (S4R in Abaqus library) with an edge length equal to gauge length of the DB specimen (70 mm) was created and loaded under uniaxial tension $\eta = 1/3$; the same approach has been employed in [11,15]. The FE model and corresponding results are shown in Fig. 14(a). Although the large shell model does not capture the softening beyond localization that leads to stiffer response compared with the test, the general trend is well captured. To be on the conservative side, fracture point was selected so that engineering fracture strain of large shell is lower than observed in test. Corresponding equivalent plastic fracture strain determined this way was$\bar{\varepsilon}_f = 0.29$ and thus, this value was used in Eq. (8) instead of $n = 0.21$. The fracture criterion is implemented in ABAQUS/Explicit VUMAT subroutines through normalized damage D indicator framework

$$D = \frac{\int_0^{\bar{\varepsilon}} d\bar{\varepsilon}}{\bar{\varepsilon}_f(\eta, t_e/L_e)} \tag{11}$$

For undeformed material $D = 0$ and $D = 1$ at fracture initiation. The corresponding fracture strain according to Eq. (6) is shown for two element lengths in Fig. 15. The applicability of the 2FS scaling is limited to multi-axial tension stress states (triaxiality of $\eta = 1/3 \ldots 2/3$) by the

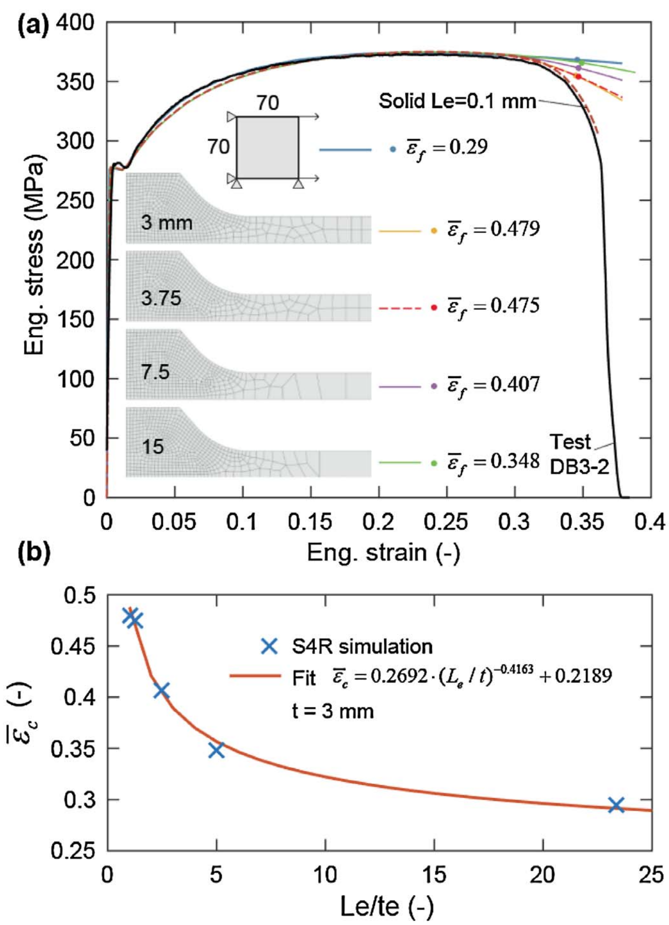

Fig. 14. (a) Shell element simulation results compared with DB3-2 experiment. The point where fracture was assumed to take place is shown with marker and plotted as a function of Le/te ratio in figure (b). (b) Cockcroft–Latham calibration parameter determined with dog-bone specimens shown in figure (a) and corresponding fit.

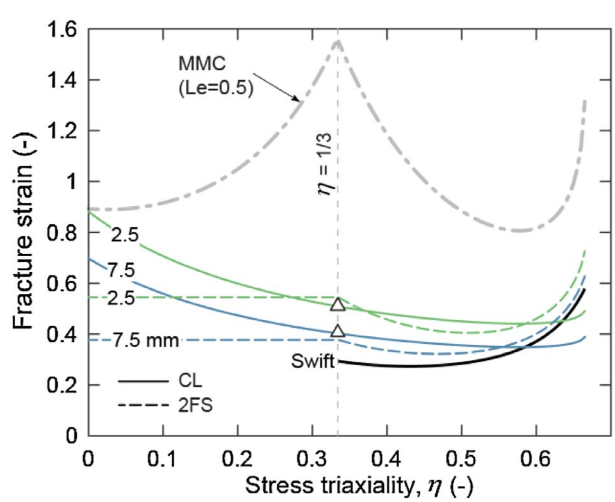

Fig. 15. Fracture strain according to two criteria: 2FS and CL. Fracture strain is shown for 2.5 mm and 7.5 mm element size. Triangular marker denotes the Cockcroft–Latham calibration parameter.

Swift diffuse necking strain. Therefore, fracture strain for the range of $-1/3 < \eta < 1/3$ was assumed to be stress state independent and the same as under uniaxial tension, $\eta = 1/3$. The practical relevance of this assumption to results was found to be negligible since analysis of simulation results showed that all elements failed under multi-axial tension regime ($\eta = 1/3 \dots 2/3$).

3.3.2. Cockcroft–Latham criterion

Comparative simulations are performed with Cockcroft–Latham (CL) criterion [44]. The sensitivity of the CL criterion to element size can be calibrated only based on the fracture strain determined with tensile test, which renders it much cheaper compared with the approach presented above. Therefore, it has been lately employed in different experimental-numerical studies, see e.g. [15,20,27]. However, compared with scaling framework introduced in previous section fracture strain adjustment for different element size is also based on single stress state. The aim is to test how this limitation affects the accuracy of the FE solution.

According to CL criterion failure occurs when integral of the maximum principal stress along the plastic strain path reaches a critical value. Wierzbicki and Werner [45] showed that the CL criterion can be expressed as a function of stress triaxiality and this formulation is adopted herein. The criterion is again implemented in the ABAQUS VUMAT subroutine through damage D indicator framework whereby element is removed from simulation once the integral of the CL damage along the plastic strain path reaches a critical value of 1. The damage in the element is given as

$$D = \frac{1}{\bar{\varepsilon}_c} \int 2 \frac{1 + \eta\sqrt{12 - 27\eta^2}}{3\eta + \sqrt{12 - 27\eta^2}} d\bar{\varepsilon} \tag{12}$$

where $\bar{\varepsilon}_c$is a calibration parameter determined with dog-bone tensile test simulations. For that purpose, dog-bone specimen was modelled with S4R (Abaqus library) shell elements with the following edge length in the loading direction: Le = 3, 3.75, 7.5 and 15 mm. Loading and boundary conditions were defined similarly to solid models shown in Fig. 12, except symmetry in thickness direction. Additionally, large shell element result from previous section was utilized in calibration. The engineering stress-strain curves from the simulations are compared with experiment in Fig. 14(a). The calibration parameter determined this way is plotted as a function of element size (L_e/t_e) in Fig. 14(b). The fit through calibration points was fed into VUMAT subroutine along with Eq. (12). The CL fracture strain is also shown for two element lengths in Fig. 15. Notice that the fracture strain at uniaxial tension ($\eta = 1/3$) provided by the 2FS framework is close to the one determined with dog-bone tests (triangular marker) and used in CL criterion calibration. Thus, two criteria yield similar fracture strain at uniaxial tension.

3.4. Finite element modelling of panels

Stiffened panel material was modelled by with von Mises J_2 flow theory. The elastic properties, flow curve and fracture criteria calibrated with tensile tests were used in the simulations. To test the strain-rate sensitivity of the panels additional simulations were performed with rate-independent flow curve – in Eq. (1) the term in square brackets [•] was removed. These simulations without strain rate dependence were performed only with 2FS criterion.

FE simulations were performed with Abaqus/Explicit version 6.13-3 using reduced integration shell elements (S4R) with default hourglass control and 5 through thickness integration points. Fig. 16 illustrates the assembly of the numerical model. Panel was the only deforming object in the analysis, while indenter, top and bottom support as well as the steel inserts were modelled with rigid material since no deformations were observed in the experiments. The reference surfaces of the face plates were off-set for best representation of the actual topology as shown in Fig. 16. In the initial configuration, the indenter was placed so that indenter hit location corresponds with SP4 panel test conditions as shown in Table 1 (x = 598 mm, y = 593 mm).

In developing the model, the adequacy of different boundary configurations, mainly the effect of modelling supports, was tested to predict the global deformations observed in the panels. As the panels exhibited some pull-out from the clamping frame during experiments, it

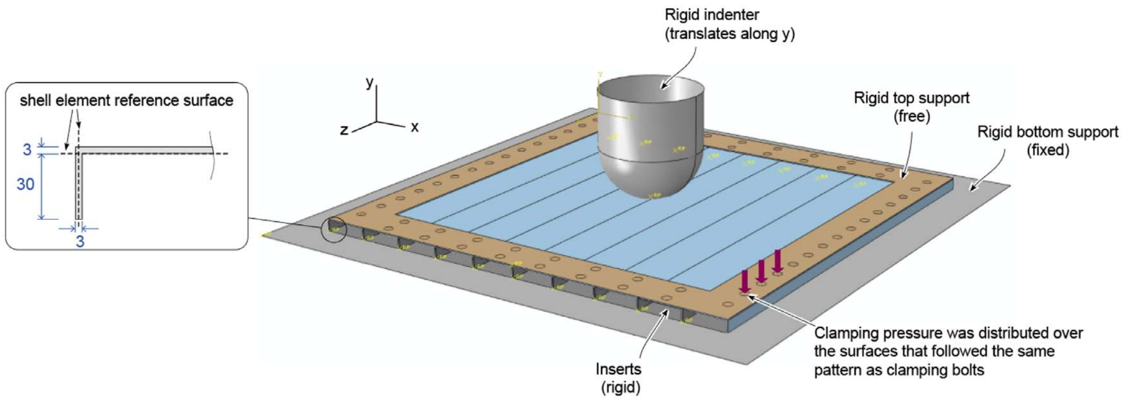

Fig. 16. General view of the stiffened panel FE model.

was included in the FE model. Clamping was implemented by distributing the total clamping force of 9 MN (see Section 2.2) between areas representing the clearance holes of the bolts in the top support. Although this clamping arrangement permitted less pull-out than observed in experiments, it was deemed sufficient as the initial stiffness of the panels was accurately represented.

Contact between different objects was modelled with general contact algorithm by defining rigid objects as masters. Contact definition included model for tangential and normal behaviour. Tangential behaviour between surfaces was modelled with penalty type friction formulation with friction coefficient of 0.23. This friction coefficient was selected based on the measurements performed in [17] who performed similar quasi-static indentation experiments with the same nominal strength steel used herein. Contact behaviour normal to surfaces was modelled with "hard" pressure-overclosure relationship. Hard contact implies that surfaces transmit contact pressure only when nodes of slave surface (panel) are in contact with master surface (indenter). The indentation experiment was simulated by assigning a same constant vertical velocity as in experiments (10 mm/min) to indenter, while constraining all other degrees of freedom. To speed up the simulations mass of the entire model was scaled by a factor of 10^7. Contact region between indenter and panel was discretized with three different element sizes to test the fracture scaling framework: $L_e = 2.5$ mm $L_e = 7.5$ mm (square shaped) and $L_e = \sqrt{A} = \sqrt{15 + 19.5} = \sim 17$ mm (rectangular elements). In rest of the model element size ranged from 10 to 15 mm.

4. Numerical results

In Fig. 17 simulated force-displacement results obtained with both criteria are compared with experimental curve. The comparison of peak force in the zoom inset of Fig. 17(a) suggests that for all the practical purposes the FE solution is strain-rate insensitive. The global stiffness of the panels is slightly overestimated during indentation, especially at higher displacement. This could be explained by the slight pull-out of the panels during experiment (less than 10 mm), which was not observed in simulations, or by the inaccuracies in calibrated flow curve. Notably, some inaccuracies were observed in modelling notched tension and shear test.

We proceed to analyze the point of fracture initiation obtained with different fracture criteria. With 2FS criterion the onset of fracture in panels represented by the load drop in Fig. 17(a) is captured with good accuracy despite the large mesh size variations. The largest discrepancy with SP4 experiment is observed in simulations with finest mesh where the peak load is overestimated by 50 kN (9%). Simulations with coarser meshes (7.5 and 17 mm) capture the experimental load drop almost perfectly. In contrast, the analysis results with CL criterion in Fig. 17(b) show larger scatter in terms of fracture initiation, which implies to less effective fracture strain scaling. While the accuracy is excellent with 2.5 mm model, coarse mesh models underestimate the peak load.

To gain further insight into the damage process snapshots of the damaged panels are shown in Fig. 18. Fracture path is independent of the fracture criterion in 2.5 mm model and very similar to SP4 experiments shown in Fig. 9(a): initially two independent cracks propagated and finally coalesced into one. 2FS criterion results in Fig. 18(a)

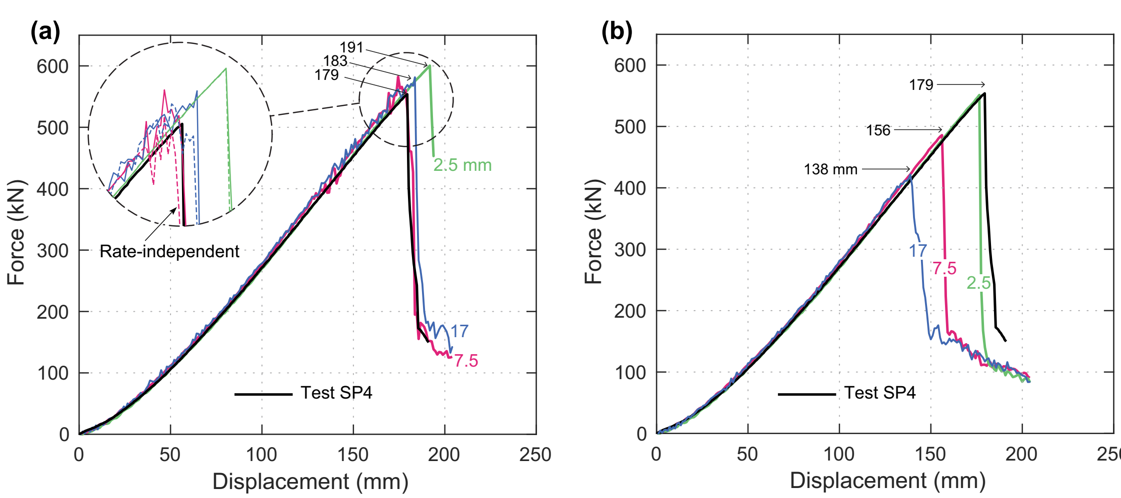

Fig. 17. Experimental force-displacement curve compared with simulation results. (a) 2FS criterion. Zoom of the peak forces shows that strain-rate strengthening (dashed curves) had minute effect on the response. (b) Cockcroft-Latham criterion.

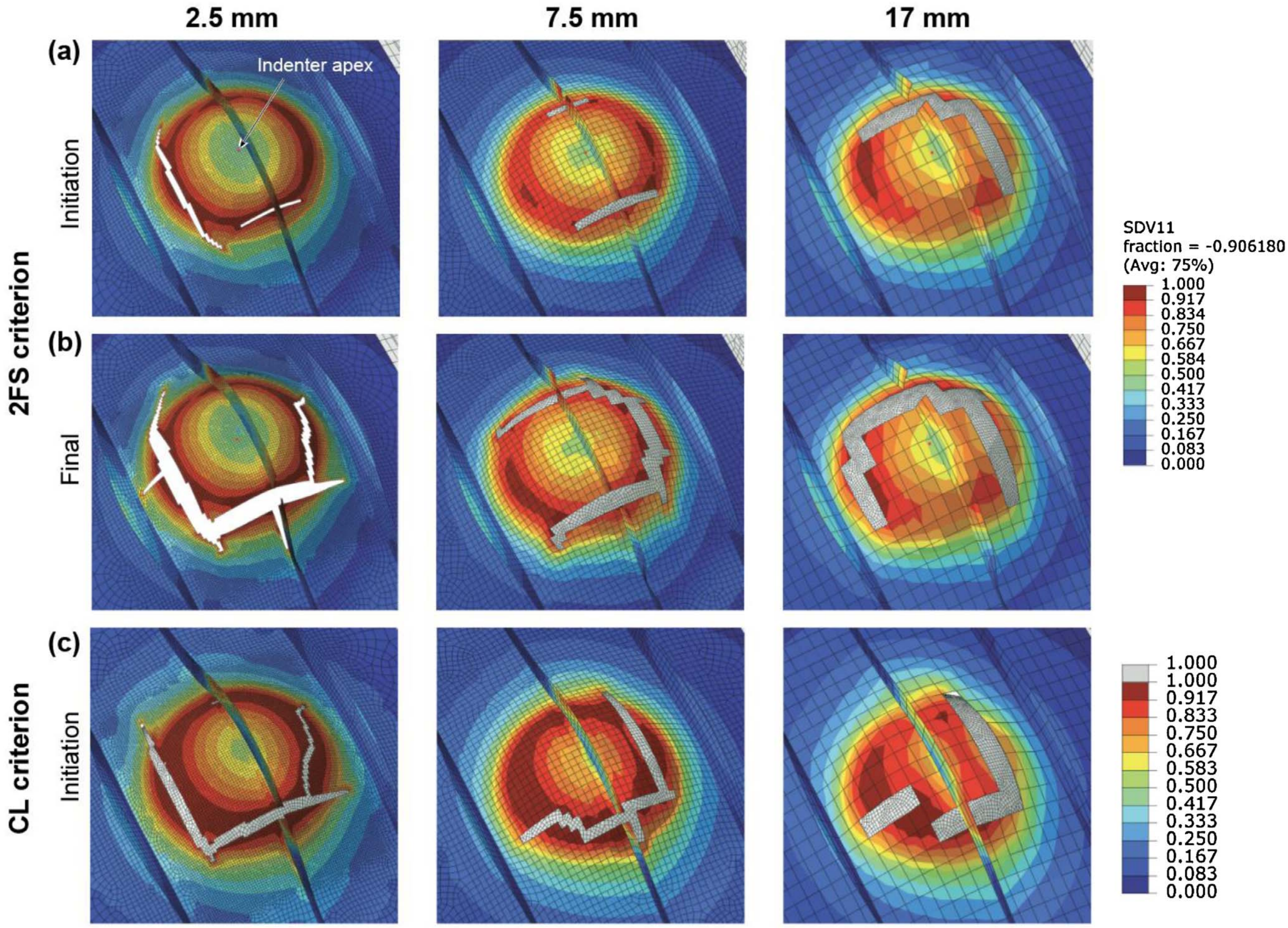

Fig. 18. Fracture propagation in stiffened panel simulations as viewed from bottom of the panels. (a) and (b) correspond to 2FS criterion and (c) shows the results of CL criterion. Color contours represent damage as calculated with Eq. (11) and Eq. (12).

and (b) show that in contrast to 2.5 mm model, the fracture in coarse mesh models initiated from the stiffener and then further into the plate field. This seems to affect also the final fracture path since in the 7.5 mm model circumferential crack propagates on the other side of the stiffener with respect to initial contact point between indenter apex and plate. In 17 mm model the final deformation pattern is also different from the one obtained with 2.5 mm model. The coarse mesh models analyzed with CL criterion in Fig. 18(c) on the other hand showed that fracture always inititated from the plate field.

The analyses of stress state in fractured elements provided explanation for discrepancy in peak load estimation between CL and 2FS criterion. The load drop in Fig. 17 was confirmed to associate with the fracture initiation in the plate field. While fracture in stiffener occurred under uniaxial tension $\eta = 1/3$, majority of plate field elements failed between stress triaxiality of 0.6 to 0.65. Despite the similarities in fracture loci plotted in Fig. 15, at these stress states 2FS criterion is less mesh size sensitive and provides slightly higher fracture strain. Therefore, the accuracy of the 2FS criterion stems from the combination of input MMC criterion and employed scaling framework. Compared with CL criterion, MMC recognizes the higher fracture ductility under equibiaxial tension while the scaling framework is able to discern reduced fracture strain sensitivity at higher stress triaxialities (0.6 to 0.65) compared with uniaxial tension.

5. Concluding remarks

The accuracy of non-linear finite element simulations to capture fracture initiation in stiffened panels is assessed under the circumstances where material fracture ductility is known over a wide range of stress states. Therefore, quasi-static indentation experiments were performed with laser-welded stiffened panels produced from standard marine structural steel. Although the relatively simple panels do not sample all the relevant deformation pathways, this apparent drawback limits the number of modelling approximations, idealizations, and assumptions. Panel material plasticity and fracture behaviour were characterized with four different tensile tests: dog-bone, central hole, notched tension, and shear specimen. The material true stress – strain curve was calibrated via inverse numerical-experimental approach using central hole specimen and validated with rest of the specimens.

In the numerical panel simulations, the element size was varied in the range of 2.5 to ~17 mm. Two fracture criteria were used. First, a criterion denoted as 2FS was employed which requires lower and upper bound stress triaxiality dependent fracture strain. As an upper bound MMC fracture criterion was fitted to the fracture data obtained through inverse approach. The fracture in panels was simulated employing a scaling framework whereby fracture strain is adjusted based on the element length and stress triaxiality. Second, Cockcroft–Latham (CL) criterion was employed. Two criteria are distinguished by way how the fracture strain scaling with respect to element size is handled. According to 2FS criterion fracture strain sensitivity to element size is dependent on stress state, while CL criterion scales fracture strain uniformly across all stress states. This expedites the calibration process compared with 2FS criterion. Nevertheless, the extra calibration effort pays off when observing the panel simulation results. The onset of fracture was captured with excellent accuracy independent of discretization length when employing 2FS criterion. In contrast, the fracture displacement and force obtained with CL criterion displayed strong mesh size dependence.

This outcome shows the important role of fracture strain scaling framework especially in the context of conceptual design where "blind" numerical testing with coarse meshes is employed to gauge the sensitivity of different designs. The drawback of the approach is its expensive scaling with multiple tensile specimens, although this cost is believed to reduce over time by development of material libraries and concurrent recognition of trends that relate fracture ductility with stress state. Furthermore, the framework is currently limited to multi-axial tension and thus, would need to be extended for other stress states. The analyses here were limited to base plate failure without considering the effect of welds and related change in material properties. These issues are left to be tackled in future investigations.

Acknowledgements

The financial support of The Scientific Advisory Board For Defence (MATINE) project with code 2500M-0058 is acknowledged with gratitude. The total funding granted to Aalto University was EUR 106795. We would also like to thank CSC – IT Centre for Science Ltd. for providing Abaqus package license and Reijo Lindgren from SIMULIA Finland for many valuable discussions regarding modelling issues. Appreciation goes also to Pauli Lehto (hardness measurements), Otto Puolakka (photos), Veijo Laukkanen, Kari Kantola, Olli Kamunen, Kim Widell (experiments), and Prof. Sven Bossuyt (DIC) analysis.

References

[1] Soares CG, Teixeira AP. Risk assessment in maritime transportation. Reliab Eng Syst Safe 2001;74:299–309.
[2] Lecklin T, Ryömä R, Kuikka S. A Bayesian network for analyzing biological acute and long-term impacts of an oil spill in the Gulf of Finland. Mar Pollut Bull 2011;62. http://dx.doi.org/10.1016/j.marpolbul.2011.08.045. 2822–35.
[3] Montewka J, Weckström M, Kujala P. A probabilistic model estimating oil spill clean-up costs - a case study for the Gulf of Finland. Mar Pollut Bull 2013;76:61–71.
[4] García Negro MC, Villasante S, Carballo Penela A, Rodríguez Rodríguez G. Estimating the economic impact of the prestige oil spill on the death coast (NW Spain) fisheries. Mar Policy 2009;33:8–23. http://dx.doi.org/10.1016/j.marpol.2008.03.011.
[5] Goerlandt F, Montewka J. A probabilistic model for accidental cargo oil outflow from product tankers in a ship-ship collision. Mar Pollut Bull 2014;79:130–44. http://dx.doi.org/10.1016/j.marpolbul.2013.12.026.
[6] Valdez Banda OA, Goerlandt F, Montewka J, Kujala P, Banda OAV, Goerlandt F, et al. A risk analysis of winter navigation in Finnish sea areas. Accid Anal Prev 2015;79:100–16. http://dx.doi.org/10.1016/j.aap.2015.03.024.
[7] Pedersen PT. Review and application of ship collision and grounding analysis procedures. Mar Struct 2010;23:241–62.
[8] Hogström P, Ringsberg JW. An extensive study of a ship's survivability after collision - a parameter study of material characteristics, non-linear FEA and damage stability analyses. Mar Struct 2012;27:1–28.
[9] Manderbacka T. Fast simulation method for transient flooding of a ship Doctoral thesis Aalto University publication series; 2015
[10] Calle MAG, Alves M. A review-analysis on material failure modeling in ship collision. Ocean Eng 2015;106:20–38. http://dx.doi.org/10.1016/j.oceaneng.2015.06.032.
[11] Woelke PB, Abboud NN. Modeling fracture in large scale shell structures. J Mech Phys Solids 2012;60:2044–63. http://dx.doi.org/10.1016/j.jmps.2012.07.001.
[12] Storheim M, Amdahl J, Martens I. On the accuracy of fracture estimation in collision analysis of ship and offshore structures. Mar Struct 2015;44:254–87.
[13] Carlebur AFC. Full-Scale Collision Tests. Saf Sci 1995;19:171–8.
[14] Wevers L, Vredeveld AW. Full scale ship collision experiments 1998 Delft: TNO; 1999. TNO-report 98-CMC-R0359.
[15] Morin D, Kaarstad BL, Skajaa B, Hopperstad OS, Langseth M. Testing and modelling of stiffened aluminium panels subjected to quasi-static and low-velocity impact loading. Int J Impact Eng 2016;0:1–15. http://dx.doi.org/10.1016/j.ijimpeng.2017.03.002.
[16] Gruben G, Morin D, Langseth M, Hopperstad OS. Strain localization and ductile fracture in advanced high-strength steel sheets. Eur J Mech A/Solids 2017;61:315–29. http://dx.doi.org/10.1016/j.euromechsol.2016.09.014.
[17] Karlsson UB, Ringsberg JW, Johnson E, Hoseini M, Ulfvarson A. Experimental and numerical investigation of bulb impact with a ship side-shell structure. Mar Technol 2009;46:16–26.
[18] Liu B, Guedes Soares C. Experimental and numerical analysis of the crushing behaviour of stiffened web girders. Int J Impact Eng 2016;88:22–38. http://dx.doi.org/10.1016/j.ijimpeng.2015.09.004.
[19] Alsos HS, Amdahl J, Hopperstad OS. On the resistance to penetration of stiffened plates, part II: numerical analysis. Int J Impact Eng 2009;36:875–87. http://dx.doi.org/10.1016/j.ijimpeng.2008.11.004.
[20] Gruben G, Sølvernes S, Berstad T, Morin D, Hopperstad OS, Langseth M. Low-velocity impact behaviour and failure of stiffened steel plates. Mar Struct 2017;54:73–91.
[21] Jones N. Structural impact. Second edition Cambridge University Press; 2012. http://dx.doi.org/10.1017/CBO9781107415324.004. vol. 1.
[22] Liu B, Villavicencio R, Soares CG. Simplified analytical method to evaluate tanker side panels during minor collision incidents. Int J Impact Eng 2015;78:20–33.
[23] Storheim M, Amdahl J. On the sensitivity to work hardening and strain-rate effects in nonlinear FEM analysis of ship collisions. Ships Offshore Struct 2017.
[24] Remes H, Varsta P. Statistics of weld geometry for laser-hybrid welded joints and its application within notch stress approach. Weld World 2010;54:R189–207.
[25] Bezensek B, Hancock JW. The toughness of laser welded joints in the ductile {\textendash}brittle transition. Eng Fract Mech 2007;74:2395–419.
[26] DNV GL AS. Rules for classification ships Edition October 2015 Part 2 Materials and welding Chapter 3 Non-metallic materials 2015:41.
[27] Wadley HNG, Borvik T, Olovsson L, Wetzel JJ, Dharmasena KP, Hopperstad OS, et al. Deformation and fracture of impulsively loaded sandwich panels. J Mech Phys Solids 2013;61:674–99. http://dx.doi.org/10.1016/j.jmps.2012.07.007.
[28] Pavlina EJ, Van Tyne CJ. Correlation of Yield strength and Tensile strength with hardness for steels. J Mater Eng Perform 2008;17:888–93. http://dx.doi.org/10.1007/s11665-008-9225-5.
[29] Gorji MB, Mohr D. Micro-tension and micro-shear experiments to characterize stress-state dependent ductile fracture. Acta Mater 2017;131:65–76. http://dx.doi.org/10.1016/j.actamat.2017.03.034.
[30] Roth CC, Mohr D. Ductile fracture experiments with locally proportional loading histories. Int J Plast 2015:1–27.
[31] Benzerga AaA, Leblond J. Ductile fracture by void growth to coalescence. Adv Appl Mech 2010;44:169–305.
[32] Till E, Hackl B. Calibration of plasticity and failure models for AHSS sheets. Proceedings of the international deep drawing research conference IDDRG 2013. 2013.
[33] Dunand M, Mohr D. Hybrid experimental-numerical analysis of basic ductile fracture experiments for sheet metals. Int J Solids Struct 2010;47:1130–43. http://dx.doi.org/10.1016/j.ijsolstr.2009.12.011.
[34] Choung J, Nam W, Lee J-Y. Dynamic hardening behaviors of various marine structural steels considering dependencies on strain rate and temperature. Mar Struct 2013;32:49–67.
[35] Gu G, Mohr D. Anisotropic Hosford-Coulomb fracture initiation model: theory and application. Eng Fract Mech 2015;147:480–97. http://dx.doi.org/10.1016/j.engfracmech.2015.08.004.
[36] Gruben G, Langseth M, Fagerholt E, Hopperstad OS. Low-velocity impact on high-strength steel sheets: an experimental and numerical study. Int J Impact Eng 2016;88:53–171. http://dx.doi.org/10.1016/j.ijimpeng.2015.10.001. 1.
[37] Bai Y, Wierzbicki T. Application of extended Mohr – Coulomb criterion to ductile fracture. Int J Fracture 2010:1–20. http://dx.doi.org/10.1007/s10704-009-9422-8.
[38] Boyce BL, Kramer SLB, Fang HE, Cordova TE, Neilsen MK, Dion K, et al. The sandia fracture challenge: blind round robin predictions of ductile tearing. Int J Fract 2014;186:5–68.
[39] Li Y, Luo M, Gerlach JJ, Wierzbicki T. Prediction of shear-induced fracture in sheet metal forming. J Mater Process Technol 2010;210:1858–69. http://dx.doi.org/10.1016/j.jmatprotec.2010.06.021.
[40] Walters CL. Framework for adjusting for both stress triaxiality and mesh size effect for failure of metals in shell structures. Int J Crashworthiness 2014;19:1–12. http://dx.doi.org/10.1080/13588265.2013.825366.
[41] Kõrgesaar M, Remes H, Romanoff J. Size dependent response of large shell elements under in-plane tensile loading. Int J Solids Struct 2014;51:3752–61. http://dx.doi.org/10.1016/j.ijsolstr.2014.07.012.
[42] Törnqvist R. Design of crashworthy ship structures Ph.D. thesis Technical University of Denmark; 2003. http://dx.doi.org/10.1007/s00726-011-1022-z.
[43] Swift HW. Plastic instability under plane stress. J Mech Phys Solids 1952;1:1–18.
[44] Cockcroft MG, Latham DJ. Ductility and the workability of metals. J Inst Met 1968;96:33–9.
[45] Wierzbicki T., Werner H. Cockcroft and Latham revisited - impact and crashworthiness laboratory report nr. 16, Technical report, MIT. 1998.